

Dynamics of Long-lived Carriers in Molybdenum Carbide Nanosheets

Xiangyu Zhu^{1,2}, Zhong Wang^{1,2}, Tao Li¹, Xi Wang^{1,2}, Zheng Zhang^{1,2}, Chunlong Hu^{1,2}, Kaifu Huo¹, Wenxi Liang^{1,2,a)}

¹Wuhan National Laboratory for Optoelectronics, Huazhong University of Science and Technology, Wuhan 430074, China

²Advanced Biomedical Imaging Facility, Huazhong University of Science and Technology, Wuhan 430074, China

^{a)}Author to whom correspondence should be addressed: wxliang@hust.edu.cn

ABSTRACT

Molybdenum carbide (MoC) is a promising candidate for substituting expensive platinum-group metals in many applications owing to its low cost and excellent properties. A comprehensive understanding of the carrier dynamics in MoC facilitates its implementations and helps designing synthesis strategies. In this work, the carrier relaxation in MoC nanosheets is investigated by combining femtosecond transient reflection spectroscopy with first-principles calculations. The observed processes of electron–electron, electron–phonon, and phonon–phonon scattering show longer lifetimes compared to those of other transition metal carbides. The nanosecond carrier lifetime is explained by the restricted phonon decay pathways induced by the large mass difference between C and Mo atoms, which is revealed through the analysis of calculated phonon dispersion. The slow cooling of hot carriers in MoC nanosheets offers a simple approach for designing devices that effectively utilize hot carriers, which are expected to improve photothermal and photovoltaic performances.

Transition metal carbides (TMCs), as the emerging members of two-dimensional (2D) material family, hold promising potentials in applications of catalysis, energy storage, flexible electronic devices, and so on,^{1,2} owing to their many excellent properties including high chemical stability and outstanding optoelectronic performance.^{3,4} In order to make better use of these materials, progresses were made in studies on mechanisms of the optical, electrical, and thermal properties of 2D TMCs. For instance, the transient absorption spectroscopy investigation of nonlinear broadband absorption of Ti_3C_2 nanosheets found that the lifetimes of electron–phonon (e–p) and phonon–phonon (p–p) interactions extended with increasing pump fluences,⁵ showing potential for applications in broadband optical limiters and novel photonic devices.⁶ Another 2D TMC, Nb_2C , which is promising for ultrafast photonic devices, exhibits stronger optical response and higher photothermal conversion efficiency than those of Ti_3C_2 ,⁷ while its carrier relaxation time is shorter than that

of graphene.⁸ So far many 2D TMCs based applications are still in their infancy, as the carrier dynamics of 2D TMCs that determine their performances are still under investigation.

In recent years, the development of alternatives to noble metals in plasmonic nanostructures attracts considerable interests.⁹ Molybdenum carbide (MoC) was extensively studied in applications of catalysis and energy storage,^{3,10} under considering its advantages of abundance, low cost, and in particular, the similar electronic structure and catalytic properties to those of platinum-group metals.¹¹ According to the calculated band structure, the work function of MoC is around 3.8 eV,¹² and the absence of band gap near Fermi level indicates its metallic properties.¹³ Additionally, the steady-state absorption spectra demonstrated strong absorption spanning a broad wavelength range from visible to near-infrared light (500–2000 nm),¹⁴ which marked MoC an excellent broadband optical material. However, the photophysical properties of MoC, particularly the hot carrier dynamics and photothermal response on ultrafast timescale, remain uncharted. The elucidation of these dynamics sets the basis for implementing MoC in applications across photovoltaics to photocatalysis.

In this work, we investigate the carrier dynamics in MoC nanosheets by employing femtosecond transient reflection (TR) spectroscopy and first-principles calculations. The bleach signals recorded in TR measurements decay in a three-stage process with lifetimes of e–p and p–p scattering on scales of hundred-picosecond and nanosecond, respectively, which are all longer than those of other TMCs, such as Nb₂C and Ti₃C₂. The phonon decay pathways accounting for the nanosecond carrier lifetime is resolved by the calculated phonon dispersion, in which we find that the large phonon band gap introduced by the large mass difference between C and Mo atoms results in the suppressed phonon decays and the subsequently extended carrier relaxation process.

The investigated samples are synthesized through a salt-assisted method (see Methods in Supplementary Materials). Their morphology, crystallization and optical response are examined by scanning electron microscopy (SEM), X-ray diffraction (XRD) and steady-state absorption spectrum, respectively, see Fig. 1. The synthesized MoC nanosheets with hexagonal lattice structure tend to agglomerate, as shown in Fig. 1(a), exhibiting large stacked areas and dispersed small fragments both with lateral dimensions ~1 μm. Under XRD examination, strong diffraction peaks that verify the hexagonal phase are observed, as shown in Fig. 1(b), as well indicating the high crystallinity of samples. The steady-state absorption spectrum shows strong absorption in the range across visible to near-infrared wavelength, as shown in Fig. 1(c), indicating the metallic nature of hexagonal MoC.

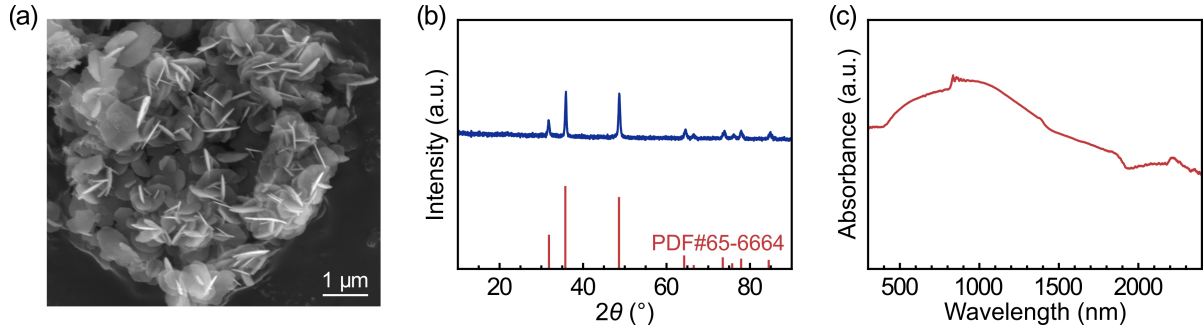


FIG. 1. Sample characterizations. (a) SEM image, showing densely stacked MoC nanosheets. The thickness of single flakes is measured to be 8–9 nm. (b) XRD pattern compared with standard PDF data, showing peaks at 31.83° , 35.75° , 48.61° , 64.23° , 66.52° , 73.48° , 75.74° , 77.88° , and 84.49° , which correspond to the (001), (100), (101), (110), (002), (111), (200), (102), and (201) crystal planes of hexagonal phase MoC. (c) Steady-state absorption spectrum.

We first examine the hot carrier relaxation by measurements with visible supercontinuum white light detection, upon excitation of 400 nm pulses (see Methods in Supplementary Materials). Under viewing by a microscope, the samples appear mainly opaque with shiny reflected light, as shown in Fig. 2(a). Fig. 2(b) and 2(c) show the pseudocolor contour plot of measured TR spectrum and the spectrum profiles at selected delay times after excitation, respectively. A broad bleach signal in visible range dominates the spectrum, matching the strong absorption observed in steady-state absorption spectrum. The bleach amplitude reaches its maximum in a few picoseconds, then decays in a process lasting more than 8 ns, showing a long carrier lifetime on nanosecond scale.

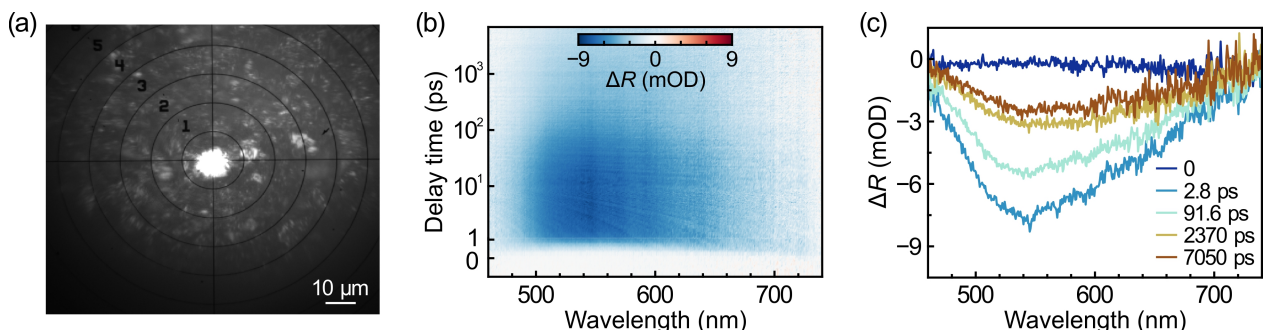


FIG. 2. TR spectroscopy measurement upon 400 nm excitation. (a) Optical photograph of the sample illustrated by excitation pulses, viewing by a microscope. (b) Pseudocolor contour plot of measured TR spectrum. (c) Spectrum profiles at selected delay times extracted from (b).

More details of bleach signal evolution are examined with various injected carrier densities. Fig. 3(a) depicts the spectra under various excitation powers, at the delay time when the bleach amplitudes reach their maximum, showing a prominent red shift of bleach peak following the increase of excitation power. Similar red shifts were also observed in metals, such as Ni, Au, Ag, and Ge,^{15–18} which were attributed to the enhanced electron–electron (e–e) scattering and e–p scattering, or band renormalization effects under high excitation

power. The maximum bleach amplitude increases as the excitation power increases, exhibiting a nearly linear dependence before approaching saturation, as depicted in the inset of Fig. 3(b). We extracted the power-dependent kinetics probed at 544 nm and fit the traces with multiexponential functions (see Supplementary Table S1 in Supplementary Materials for tabulated fit results), finding that the decay processes show a three-stage evolution, as depicted in Fig. 3(b). The bleach decay reflects that the excited carriers in MoC relax in three stages with lifetimes of several tens of picoseconds, a few nanoseconds, and several nanoseconds beyond the measured time window, respectively. Compared to the carrier lifetimes of other 2D materials, e.g., a few picoseconds of graphene¹⁹ and a few hundred picoseconds of MoS₂²⁰ and WS₂,²¹ the carrier lifetime of MoC is significantly longer.

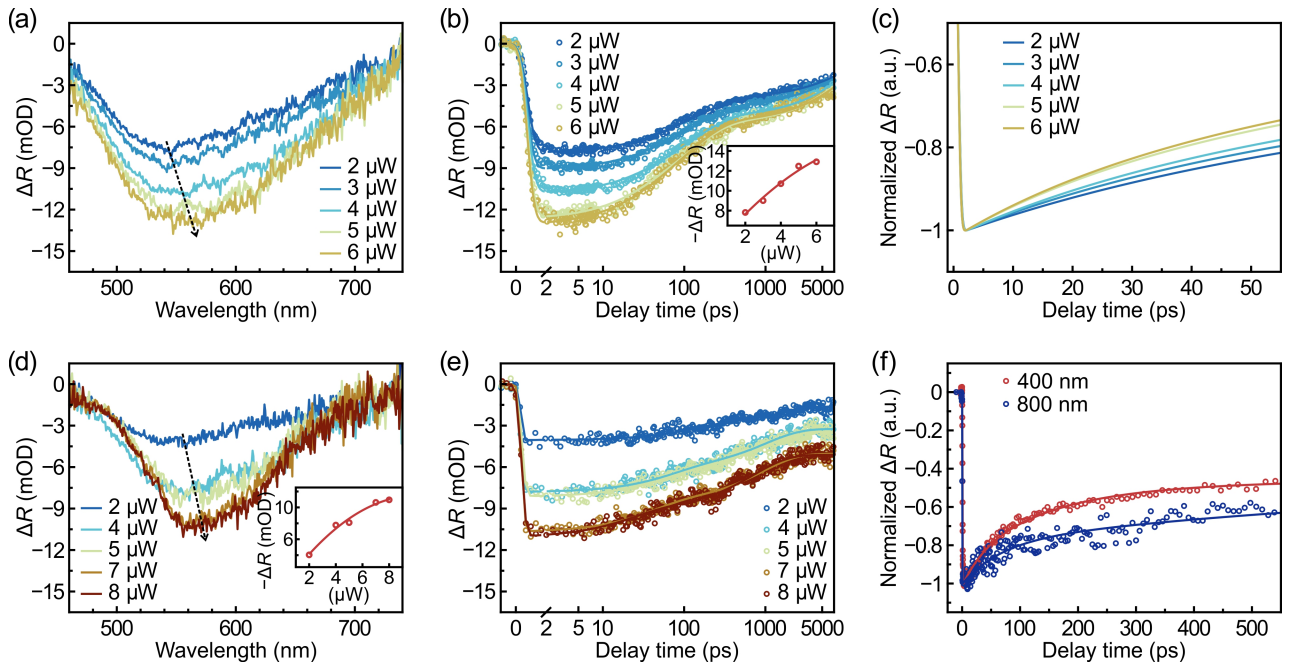


FIG. 3. Carrier relaxation upon 400 nm (a–c) and 800 nm (d–e) excitations with various powers. (a, d) Change of spectrum profiles following the increase of excitation power. Dashed arrow, the guide to the eyes. Inset in (d), saturating trend of the maximum bleach amplitudes; Solid line, the guide to the eyes. (b, e) Power-dependent kinetics probed at 544 and 562 nm, respectively. Solid lines, triexponential function fits. Inset in (b), saturating trend of the maximum bleach amplitudes; Solid line, the guide to the eyes. (c) Normalized fit curves in (b) at early several tens of picoseconds. (f) Comparison between the bleach decays excited by 400 nm and 800 nm, with the same excitation power of 4 μ W. Solid lines, triexponential function fits.

In metallic materials, there are three common processes in transient responses to photoexcitation,²² i.e., e–e scattering, e–p scattering, and p–p scattering or heat diffusion, following the sequence of their occurrences. In transient absorption or TR measurements, the e–e scattering is manifested as the rise process of bleach kinetics trace, with characteristic rise time on the order of tens to hundreds of femtoseconds for metals and metal compounds, or materials with metallic properties, such as Au, Ag, Al, TiN, and ZrN.^{23–25} In our case of

MoC, the characteristic rise time (τ_0) varies from \sim 500 femtoseconds (upon 400 nm excitation, see Supplementary Table S1) to a maximum of one picosecond (upon 800 nm excitation, see later discussions), indicating a prominently slowed electron equilibration rate, which is benefit to maintain a hot carrier population for extraction before the excited electrons loss their excess energy.

With increasing excitation power, the early decay of bleach signals shows a boosted trend, as demonstrated by the normalized fit curves in Fig. 3(c). The extracted lifetimes of the first stage of carrier relaxation (τ_1) decreases with increasing injected carrier density, as summarized in Supplementary Table S1, demonstrating the feature of Auger recombination or e–p scattering process. However, the Auger recombination in 2D materials usually occurs on a faster timescale,^{26,27} therefore we attribute this stage to e–p scattering. The measured decays are slow compared to those in metals or similar materials,^{25,28} indicating a lower e–p scattering rate that leads to an extended carrier relaxation process in MoC nanosheets. The fitted weight of τ_1 is apparently larger than those of τ_2 and τ_3 (see Supplementary Table S1), indicating the dominance of e–p scattering during the carrier relaxation, i.e., more electrons release their extra energy through the channel of directly coupling to lattice.

Following the e–p scattering, the possible p–p scattering or heat diffusion for the second stage of carrier relaxation also shows decreasing lifetime (τ_2 , see Supplementary Table S1) with increasing excitation power. This boosted rate, agreeing with the acceleration of thermalization under increased injected carrier density,²⁹ is attributed to the increased p–p scattering rate as the phonon population grows,³⁰ which also introduced an increased final temperature of lattice. The longest decay lasts several nanoseconds (τ_3), representing a carrier lifetime that is significantly longer than those of other TMCs, e.g., a few picoseconds in Nb₂C³¹ and around ten picoseconds in Ti₃C₂.³² Such a long lifetime is similar to the long decay times observed in HfN³³ and BAs³⁴ nanosheets. In HfN and BAs, there are significant phonon band gaps between optical branches (OBs) and acoustic branches (ABs) due to the large mass difference between N (B) and Hf (As) atoms. As OBs are associated to displacements of light atoms while ABs are dominated by displacements of heavy atoms,³⁵ these gaps limit the pathways for optical phonons (OPs) decaying into acoustic phonons (APs), resulting in the extra energy of OPs re-scattering back to electrons, i.e., the occurrence of phonon bottleneck³⁴. Given the large mass difference between C and Mo atoms, the energy and momentum conservations also restrict the phonons decay from OBs into ABs in MoC, see discussions later. As a result, the relaxation process of photoexcited carriers extends to nanosecond scale.

Then we investigate the impact of initial electron temperature on relaxation process by comparing the TR responses upon excitations of 400 nm and 800 nm pulses. Fig. 3(d) depicts the spectra with maximum bleach amplitude under various excitation powers of 800 nm, showing the broadband but narrowed profiles compared to those upon 400 nm excitation. A red shift following the increase of excitation power is also

observed, similar to the shift in 400 nm cases. Comparing to 400 nm excitation, the maximum bleach amplitude upon 800 nm excitation approaches faster to saturation when the excitation power increases, as depicted in the inset of Fig. 3(d). Moreover, the amplitudes excited by 800 nm with same powers (2, 4 and 5 μW) are apparently smaller than those excited by 400 nm. This difference originates from the deferent changes of electron temperature after photoexcitation, as the recorded reflectivity varies linearly with electron temperature.^{25,36} Again, the bleach signal excited by 800 nm shows a three-stage decay (see Fig. 3(e) for the kinetics extracted at 562 nm), with the lifetimes of the first two stages also decreasing as the excitation power increases (see Supplementary Table S2 in Supplementary Materials for tabulated fit results). These two decays are slower than those upon 400 nm excitation, as depicted in Fig. 3(f). Furthermore, the fitted weight of the first decay is significantly smaller than those upon 400 nm excitation. Both the extended lifetime and the decreased weight of the first decay indicate that e–p scattering processes are retarded with lower initial electron temperature.

The difference of carrier relaxations under varied excitation energies can be understood in the scenario of interaction between carrier and phonon. Compared to absorbing 800 nm photons, the electrons excited by 400 nm populate further away from the Fermi level, leading to a higher electron temperature than a higher lattice temperature given the same excitation power, through a higher e–p scattering rate.^{37–39} The increased rate is attributed to that the high-energy excitation allows for efficient emissions of OPs during carrier relaxation, making the rapid scattering channel with OPs the dominant pathway,⁴⁰ while the low-energy excitation restricts the carrier relaxation to the slow scattering channel with APs.⁴¹ Moreover, both the e–p and p–p scattering processes show a trend that their lifetimes gradually stabilize with increasing excitation power, as depicted in Fig. 4. Such a trend may be interpreted by the enhanced hot-phonon bottleneck effect upon high excitation power.^{42,43} With high injected carrier density, a high phonon emission rate results in a non-equilibrium phonon population,^{44,45} which increases the phonon reabsorption rate and reduces the thermalization rate (or phonon emission rate).⁴² When the injected carrier density increases, the phonon bottleneck effect competes with the accelerated electron and lattice thermalizations, leading to the eventually converged lifetimes of carrier relaxation.

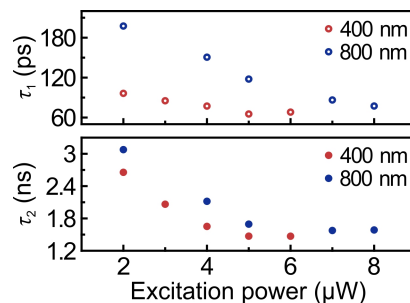


FIG. 4. Convergence of e–p and p–p scattering times following the increase of excitation power, see text.

The carrier relaxation pathways in MoC nanosheets is further elucidated by the calculated phonon dispersion through first-principles calculations with a monolayer configuration (see Methods in Supplementary Materials). As depicted in Fig. 5, the phonon dispersion shows no imaginary frequency mode and the highest vibration frequency of 21.9 THz at OBs, suggesting the dynamical stability of MoC nanosheets.⁴⁶ A large phonon band gap, which is significantly larger than those of well-studied 2D transition metal sulfides such as WS and WSe,⁴⁷ is revealed between the minimum of OBs and the maximum of ABs. This large gap, in which the highest frequency of ABs is lower than half the lowest frequency of OBs, is probably induced by the large mass difference between C and Mo atoms, similar to the discussed cases of HfN and BAs. Subsequently, the gap results in the suppressed phonon decay and the occurrence of phonon bottleneck, which in turn hinder the carrier relaxation.

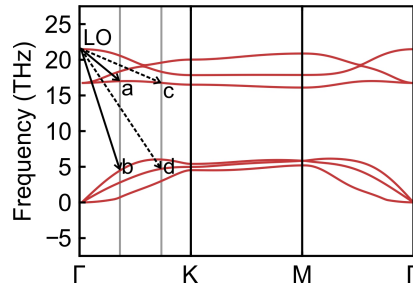


FIG. 5. Calculated phonon dispersion of monolayer MoC. Arrows, possible decay pathways of LO phonons with high frequency, see text.

Specifically, the decay of longitudinal optical (LO) phonons lays significant impacts on the carrier relaxation, as the Fröhlich interaction between carriers and LO phonons is the primary carrier–phonon scattering mechanism in polar materials.⁴⁸ Under the condition of energy and momentum conservation, the lattice anharmonicity allows for LO phonons decaying into phonons with lower frequency through various mechanisms, such as three-phonon processes,⁴⁹ in which one LO phonon decays into two phonons.^{50–52} In general, three-phonon interactions are slower than processes of LO phonon emission through carrier coupling, and the strength of higher-order processes are much weaker by order of magnitude.^{53,54} Due to the large phonon band gap and the flat OP dispersion, the channels for generating two low-frequency phonons in the same band, e.g., the Klemens channel,^{50,55} are suppressed. Additionally, the distinct splitting of LO and transvers optical branches around Γ point facilitates the Ridley–Gupta channel,^{51,56} i.e., one LO phonon decays into one OP and one AP. For possible decay pathways, we draw two lines (grey) parallel to the y-axis of calculated dispersion, intersecting the OBs and ABs at points a, c and b, d (see Fig. 5), respectively. The summed frequencies of a and b (c and d) are equal to the highest frequency at Γ point, ensuring energy conservation. Therefore, the LO phonons with the highest frequency may possibly decay into points a and b, or into points c and d, with opposite wave vectors governed by momentum conservation, undergoing the slow three-phonon processes.

Since both the frequencies of a and c are higher than twofold the highest frequency of ABs, the phonons decayed into a or c subsequently decay to ABs through four-phonon or higher-order processes, yielding even more significantly slowed interaction processes.

Thus, the carrier relaxation in MoC nanosheets is outlined as following. Initially, photoexcited carriers transit into high-energy states and rapidly achieve a quasi-equilibrium distribution through e–e scattering. Then the hot carriers transfer their energies to lattice through e–p coupling in tens to hundreds of picoseconds, basing on the initially excited carrier temperature. Subsequently, the phonons with high frequency primarily decay into low-energy phonons through the slow channels of multiple-phonon interactions on time scale of nanosecond, at the end resulting in the observed long-lived carriers with lifetime beyond the measured time window.

In summary, the relaxation of photoexcited carriers in MoC nanosheets is elucidated by combining femtosecond TR measurements and first-principles calculations. The revealed slow carrier relaxation originates from the suppressed e–p and p–p scattering, possibly accompanied with phonon bottleneck, due to the large phonon band gap. The long-lived carriers make possible implementing MoC nanosheets in photothermal applications by designing devices that efficiently utilize hot carriers, and in photovoltaics applications by serving as an absorbing material for potential hot-carrier solar cells, in which the slow cooling of hot carriers is a key factor for better carrier extraction.

ACKNOWLEDGMENTS

We thank the Analytical and Testing Center in Huazhong University of Science and Technology for support. T.L. and K.H. thank the National Natural Science Foundation of China (52572225 and U2004210) for support.

AUTHOR DECLARATIONS

Conflict of Interest

The authors have no conflicts to disclose.

Author Contributions

X.Z. and W.L. conceived of the project. X.Z. performed the measurements with supports from X.W., Z.Z., and C.H. T.L. synthesized the MoC nanosheets under the supervision from K.H. Z.W. performed the first-principles calculations. X.Z. and W.L. analyzed the data with discussions with all authors. X.Z. and W.L. wrote the paper with contributions from all authors. W. L. supervised the project.

DATA AVAILABILITY

The data that support the findings of this study are available from the corresponding author upon

reasonable request.

REFERENCES:

¹B. Anasori, M. R. Lukatskaya, and Y. Gogotsi, “2D metal carbides and nitrides (MXenes) for energy storage,” *Nat. Rev. Mater.* **2**(2), 16098 (2017).

²K. Hantanasirisakul and Y. Gogotsi, “Electronic and optical properties of 2D transition metal carbides and nitrides (MXenes),” *Adv. Mater.* **30**(52), 1804779 (2018).

³T. Qin, Z. Wang, Y. Wang, F. Besenbacher, M. Otyepka, and M. Dong, “Recent progress in emerging two-dimensional transition metal carbides,” *Nano-Micro Lett.* **13**(1), 183 (2021).

⁴D. Zhang, D. Shah, A. Boltasseva, and Y. Gogotsi, “MXenes for photonics,” *ACS Photonics* **9**(4), 1108–1116 (2022).

⁵Y. Shao, C. Chen, Q. He, W. Wu, C. Li, and Y. Gao, “Broadband visible nonlinear absorption and ultrafast dynamics of the Ti_3C_2 nanosheet,” *Nanomaterials* **10**(12), 2544 (2020).

⁶G. Liu, J. Yuan, Z. Wu, P. Yu, Z. Wang, and X. Xu, “Deep ultraviolet optical limiting materials: 2D Ti_3C_2 and Ti_3AlC_2 nanosheets,” *J. Mater. Chem. C* **11**(6), 2355–2363 (2023).

⁷H. Lin, S. Gao, C. Dai, Y. Chen, and J. Shi, “A two-dimensional biodegradable niobium carbide (MXene) for photothermal tumor eradication in NIR-I and NIR-II biowindows,” *J. Am. Chem. Soc.* **139**(45), 16235–16247 (2017).

⁸L. Gao, H. Chen, F. Zhang, S. Mei, Y. Zhang, W. Bao, C. Ma, P. Yin, J. Guo, X. Jiang, S. Xu, W. Huang, X. Feng, F. Xu, S. Wei, and H. Zhang, “Ultrafast relaxation dynamics and nonlinear response of few-layer niobium carbide MXene,” *Small Methods* **4**(8), 2000250 (2020).

⁹Z. Chen, M. Yang, Y. Li, W. Gong, J. Wang, T. Liu, C. Zhang, S. Hou, G. Yang, H. Li, Y. Jin, C. Zhang, Z. Tian, F. Meng, and Y. Cui, “Termination-acidity tailoring of molybdenum carbides for alkaline hydrogen evolution reaction,” *Nat. Commun.* **16**(1), 418 (2025).

¹⁰C. Wang, X. Li, H. Song, P. K. Chu, and K. Huo, “In-plane heterostructured MoN/MoC nanosheets with enhanced interfacial charge transfer for superior pseudocapacitive storage,” *Adv. Funct. Mater.* **34**(12), 2311040 (2024).

¹¹C. Yang, R. Zhao, H. Xiang, J. Wu, W. Zhong, W. Li, Q. Zhang, N. Yang, and X. Li, “Ni-activated transition metal carbides for efficient hydrogen evolution in acidic and alkaline solutions,” *Adv. Energy Mater.* **10**(37), 2002260 (2020).

¹²A. A. Rouse, J. B. Bernhard, E. D. Sosa, and D. E. Golden, “Field emission from molybdenum carbide,” *Appl. Phys. Lett.* **76**(18), 2583–2585 (2000).

¹³S. T. Oyama, “Preparation and catalytic properties of transition metal carbides and nitrides,” *Catal. Today* **15**(2), 179–200. (1992).

¹⁴M. Tuo, C. Xu, H. Mu, X. Bao, Y. Wang, S. Xiao, W. Ma, L. Li, D. Tang, H. Zhang, M. Premaratne, B. Sun, H.-M. Cheng, S. Li, W. Ren, and Q. Bao, “Ultrathin 2D transition metal carbides for ultrafast pulsed fiber lasers,” *ACS Photonics* **5**(5), 1808–1816 (2018).

¹⁵H.-T. Chang, A. Guggenmos, S. K. Cushing, Y. Cui, N. U. Din, S. R. Acharya, I. J. P. Molesky, U. Kleineberg, V. Turkowski, T. S. Rahman, D. M. Neumark, and S. R. Leone, “Electron thermalization and relaxation in laser-heated nickel by few-femtosecond core-level transient absorption spectroscopy,” *Phys. Rev. B* **103**(6), 064305 (2021).

¹⁶X. Zhang, C. Huang, M. Wang, P. Huang, X. He, and Z. Wei, “Transient localized surface plasmon induced by femtosecond interband excitation in gold nanoparticles,” *Sci. Rep.* **8**(1), 10499 (2018).

¹⁷A. Gaál, I. Bugár, I. Capek, L. Fialová, T. Pálszegi, V. Szocs, A. Šatka, and F. Uherek, “Femtosecond multicolor transient absorption spectroscopy of colloidal silver nanoparticles,” *Laser Phys.* **19**(5), 961–968 (2009).

¹⁸M. Zürch, H.-T. Chang, L. J. Borja, P. M. Kraus, S. K. Cushing, A. Gandman, C. J. Kaplan, M. H. Oh, J. S. Prell, D. Prendergast, C. D. Pemmaraju, D. M. Neumark, and S. R. Leone, “Direct and simultaneous observation of ultrafast electron and hole dynamics in germanium,” *Nat. Commun.* **8**(1), 15734 (2017).

¹⁹F. Gesuele, “Ultrafast hyperspectral transient absorption spectroscopy: Application to single layer graphene,” *Photonics* **6**(3), 95 (2019).

²⁰H. Shi, R. Yan, S. Bertolazzi, J. Brivio, B. Gao, A. Kis, D. Jena, H. G. Xing, and L. Huang, “Exciton dynamics in suspended monolayer and few-layer MoS₂ 2D crystals,” *ACS Nano* **7**(2), 1072–1080 (2013).

²¹V. Vega-Mayoral, D. Vella, T. Borzda, M. Prijatelj, I. Tempra, E. A. A. Pogna, S. Dal Conte, P. Topolovsek, N. Vujicic, G. Cerullo, D. Mihailovic, and C. Gadermaier, “Exciton and charge carrier dynamics in few-layer WS₂,” *Nanoscale* **8**(10), 5428–5434 (2016).

²²G. V. Hartland, “Optical studies of dynamics in noble metal nanostructures,” *Chem. Rev.* **111**(6), 3858–3887 (2011).

²³N. Del Fatti, R. Bouffanais, F. Vallée, and C. Flytzanis, “Nonequilibrium electron interactions in metal films,” *Phys. Rev. Lett.* **81**(4), 922–925 (1998).

²⁴M.-N. Su, C. J. Ciccarino, S. Kumar, P. D. Dongare, S. A. H. Jebeli, D. Renard, Y. Zhang, B. Ostovar, W.-S. Chang, P. Nordlander, N. J. Halas, R. Sundararaman, P. Narang, and S. Link, “Ultrafast electron dynamics in single aluminum nanostructures,” *Nano Lett.* **19**(5), 3091–3097 (2019).

²⁵B. T. Diroll, S. Saha, V. M. Shalaev, A. Boltasseva, and R. D. Schaller, “Broadband ultrafast dynamics of refractory metals: TiN and ZrN,” *Adv. Opt. Mater.* **8**(19), 2000652 (2020).

²⁶W. Lin, Y. Shi, X. Yang, J. Li, E. Cao, X. Xu, T. Pullerits, W. Liang, and M. Sun, “Physical mechanism on exciton–plasmon coupling revealed by femtosecond pump–probe transient absorption spectroscopy,” *Mater. Today Phys.* **3**, 33–40 (2017).

²⁷W. Wang, N. Sui, X. Chi, Z. Kang, Q. Zhou, L. Li, H. Zhang, J. Gao, and Y. Wang, “Investigation of hot carrier cooling dynamics in monolayer MoS₂,” *J. Phys. Chem. Lett.* **12**(2), 861–868 (2021).

²⁸T. Wang, C. Yao, R. Gao, M. Holicky, B. Hu, S. Liu, S. Wu, H. Kim, H. Ning, F. Torrisi, and A. A. Bakulin, “Ultrafast Carrier and Lattice Cooling in Ti₂CT_x MXene Thin Films,” *Nano Lett.* **24**(51), 16333–16341 (2024).

²⁹F. Kurtz, T. N. Dauwe, S. V. Yalunin, G. Storeck, J. G. Horstmann, H. Böckmann, and C. Ropers, “Non-thermal phonon

dynamics and a quenched exciton condensate probed by surface-sensitive electron diffraction,” *Nat. Mater.* **23**(7), 890–897 (2024).

³⁰G. Fugallo, M. Lazzeri, L. Paulatto, and F. Mauri, “*Ab initio* variational approach for evaluating lattice thermal conductivity,” *Phys. Rev. B* **88**(4), 045430 (2013).

³¹Y. Wang, Y. Wang, K. Chen, K. Qi, T. Xue, H. Zhang, J. He, and S. Xiao, “Niobium carbide MXenes with broad-band nonlinear optical response and ultrafast carrier dynamics,” *ACS Nano* **14**(8), 10492–10502 (2020).

³²E. Colin-Ulloa, A. Fitzgerald, K. Montazeri, J. Mann, V. Natu, K. Ngo, J. Uzarski, M. W. Barsoum, and L. V. Titova, “Ultrafast spectroscopy of plasmons and free carriers in 2D MXenes,” *Adv. Mater.* **35**(8), 2208659 (2023).

³³S. Chung, X. Wen, S. Huang, N. Gupta, G. Conibeer, S. Shrestha, T. Harada, and T. W. Kee, “Nanosecond long excited state lifetimes observed in hafnium nitride,” *Sol. Energy Mater. Sol. Cells* **169**, 13–18 (2017).

³⁴U. Choudhry, F. Pan, X. He, B. Shaheen, T. Kim, R. Gnabasik, G. A. Gamage, H. Sun, A. Ackerman, D.-S. Yang, Z. Ren, and B. Liao, “Persistent hot carrier diffusion in boron arsenide single crystals imaged by ultrafast electron microscopy,” *Matter* **6**(1), 206–216 (2023).

³⁵B. Saha, J. Acharya, T. D. Sands, and U. V. Waghmare, “Electronic structure, phonons, and thermal properties of ScN, ZrN, and HfN: A first-principles study,” *J. Appl. Phys.* **107**(3), 033715 (2010).

³⁶S. D. Brorson, A. Kazeroonian, J. S. Moodera, D. W. Face, T. K. Cheng, E. P. Ippen, M. S. Dresselhaus, and G. Dresselhaus, “Femtosecond room-temperature measurement of the electron–phonon coupling constant γ in metallic superconductors,” *Phys. Rev. Lett.* **64**(18), 2172–2175 (1990).

³⁷N. Del Fatti, C. Voisin, M. Achermann, S. Tzortzakis, D. Christofilos, and F. Vallée, “Nonequilibrium electron dynamics in noble metals,” *Phys. Rev. B* **61**(24), 16956–16966 (2000).

³⁸E. V. Chulkov, A. G. Borisov, J. P. Gauyacq, D. Sánchez-Portal, V. M. Silkin, V. P. Zhukov, and P. M. Echenique, “Electronic excitations in metals and at metal surfaces,” *Chem. Rev.* **106**(10), 4160–4206 (2006).

³⁹B. Y. Mueller and B. Rethfeld, “Relaxation dynamics in laser-excited metals under nonequilibrium conditions,” *Phys. Rev. B* **87**(3), 035139 (2013).

⁴⁰S. Winnerl, M. Orlita, P. Plochocka, P. Kossacki, M. Potemski, T. Winzer, E. Malic, A. Knorr, M. Sprinkle, C. Berger, W. A. de Heer, H. Schneider, and M. Helm, “Carrier relaxation in epitaxial graphene photoexcited near the Dirac point,” *Phys. Rev. Lett.* **107**(23), 237401 (2011).

⁴¹M. W. Graham, S.-F. Shi, Z. Wang, D. C. Ralph, J. Park, and P. L. McEuen, “Transient absorption and photocurrent microscopy show that hot electron supercollisions describe the rate-limiting relaxation step in graphene,” *Nano Lett.* **13**(11), 5497–5502 (2013).

⁴²Y. Yang, D. P. Ostrowski, R. M. France, K. Zhu, J. van de Lagemaat, J. M. Luther, and M. C. Beard, “Observation of a hot-phonon bottleneck in lead-iodide perovskites,” *Nat. Photonics* **10**(1), 53–59 (2016).

⁴³S. Biswas, R. Zhao, F. Alowa, M. Zacharias, S. Sharifzadeh, D. F. Coker, D. S. Seferos, and G. D. Scholes, “Exciton

polaron formation and hot-carrier relaxation in rigid Dion–Jacobson-type two-dimensional perovskites,” *Nat. Mater.* **23**(7), 937–943 (2024).

⁴⁴W. Pötz, “Hot-phonon effects in bulk GaAs,” *Phys. Rev. B* **36**(9), 5016–5019 (1987).

⁴⁵W. W. Rühle, K. Leo, and E. Bauser, “Cooling of a hot electron-hole plasma in $\text{Al}_x\text{Ga}_{1-x}\text{As}$,” *Phys. Rev. B* **40**(3), 1756–1761 (1989).

⁴⁶Y. Wang, Y. Zhou, X.-P. Liu, Z.-Y. Zeng, C.-E. Hu, and X.-R. Chen, “Thermoelectric properties of MoC monolayers from first-principles calculations,” *AIP Adv.* **10**(12), 125220 (2020).

⁴⁷A. Samad, H. J. Kim, and Y.-H. Shin, “Stability, spontaneous and induced polarization in monolayer MoC, WC, WS, and WSe,” *J. Phys-Condens. Matter* **31**(4), 045301 (2019).

⁴⁸S. Usher and G. P. Srivastava, “Theoretical study of the anharmonic decay of nonequilibrium LO phonons in semiconductor structures,” *Phys. Rev. B* **50**(19), 14179–14186 (1994).

⁴⁹Y. Zou, H. Esmaielpour, D. Suchet, J.-F. Guillemoles, and S. M. Goodnick, “The role of nonequilibrium LO phonons, Pauli exclusion, and intervalley pathways on the relaxation of hot carriers in InGaAs/InGaAsP multi-quantum-wells,” *Sci. Rep.* **13**(1), 5601 (2023).

⁵⁰P. G. Klemens, “Anharmonic decay of optical phonons,” *Phys. Rev.* **148**(2), 845–848 (1966).

⁵¹B. K. Ridley and R. Gupta, “Nonelectronic scattering of longitudinal-optical phonons in bulk polar semiconductors,” *Phys. Rev. B* **43**(6), 4939–4944 (1991).

⁵²F. Vallée and F. Bogani, “Coherent time-resolved investigation of LO-phonon dynamics in GaAs,” *Phys. Rev. B* **43**(14), 12049–12052 (1991).

⁵³D. J. Ecsedy and P. G. Klemens, “Thermal resistivity of dielectric crystals due to four-phonon processes and optical modes,” *Phys. Rev. B* **15**(12), 5957–5962 (1977).

⁵⁴S. Barman and G. P. Srivastava, “Lifetime of nonequilibrium zone-center longitudinal optical phonons in zinc-blende materials,” *Appl. Phys. Lett.* **81**(18), 3395–3397 (2002).

⁵⁵H. Levard, S. Laribi, and J.-F. Guillemoles, “Phonon lifetime in SiSn and its suitability for hot-carrier solar cells,” *Appl. Phys. Lett.* **104**(22), 222106 (2014).

⁵⁶S. Barman and G. P. Srivastava, “Long-wavelength nonequilibrium optical phonon dynamics in cubic and hexagonal semiconductors,” *Phys. Rev. B* **69**(23), 235208 (2004).

Supplementary Materials for
Dynamics of Long-lived Carriers in Molybdenum Carbide Nanosheets

Xiangyu Zhu^{1,2}, Zhong Wang^{1,2}, Tao Li¹, Xi Wang^{1,2}, Zheng Zhang^{1,2}, Chunlong Hu^{1,2}, Kaifu Huo¹, Wenxi Liang^{1,2,*}

¹Wuhan National Laboratory for Optoelectronics, Huazhong University of Science and Technology, Wuhan 430074, China

²Advanced Biomedical Imaging Facility, Huazhong University of Science and Technology, Wuhan 430074, China

*Author to whom correspondence should be addressed: wxliang@hust.edu.cn

Methods

Sample preparation and characterization. The samples of MoC nanosheet were prepared by a Na₂CO₃-assisted annealing treatment in Ar/H₂ atmosphere, with natural molybdenite (bulk MoS₂) as the molybdenum precursor and urea as the carbon precursor. The obtained MoC nanosheets were dispersed in ethanol and transferred onto a glass slide, then dried at 80°C for 5 minutes before measurements.

The morphology of samples was examined using a field emission scanning electron microscope (Nova Nano SEM 450, FEI). The crystal structure was examined using an X-ray diffractometer (X’Pert3 Powder, PANalytical B.V.). The steady-state absorption spectrum was measured using an ultraviolet-visible-near-infrared spectrophotometer (SolidSpec-3700, Shimadzu).

Transient reflectivity spectroscopy. The TR measurements were performed using a femtosecond transient absorption spectrometer (Helios, Ultrafast Systems) with microscope extension. The output of femtosecond laser (800 nm, 40 fs, operating at a repetition rate of 5 kHz, Legend Elite, Coherent), were divided into two beams. One beam with the major part of energy was introduced into an optical parametric amplifier (TOPAS, Light Conversion) to generate pump pulses tunable in 240–2700 nm, which were then modulated by a mechanical chopper. The other beam with the small part of energy passed through a delay line to introduce optical path difference, then through a sapphire crystal to generate probe pulses of white-light continuum with wavelength of 420–820 nm. The pump and probe pulses were closely focused on the sample through a microscope objective in a near-axis configuration. The pump and probe spots on sample surface, with radius focused to 4 and 3 μm, respectively, were monitored by a charge coupled device (CCD) camera. At the end, the reflectivity signals were recorded by a linear array CCD sensor. The temporal resolution of the whole system was estimated to be ~140 fs by cross-phase modulation measurements.

First-principles calculations. The calculations of geometry optimization of monolayer MoC were performed using the Vienna *ab initio* simulation package (VASP) code¹ with the generalized gradient approximation

(GGA) of Perdew–Burke–Ernzerhof (PBE). The projector augmented wave (PAW) method was utilized with a plane-wave basis set,² and the convergence criteria were set to 10^{-8} eV for energy and 10^{-6} eV/Å for force. A kinetic cutoff energy of 400 eV and a Monkhorst–Pack³ special k-point mesh of $11 \times 11 \times 2$ were employed for the calculations. A vacuum layer with thickness of 15 Å was used in monolayer MoC to avoid interactions between adjacent monolayers. The phonon properties were obtained from the density functional perturbation theory using the Phonopy software package⁴ and a $4 \times 4 \times 1$ supercell.

Supplementary Tables

TABLE S1. Fit results of the kinetics probed at 544 nm upon 400 nm excitation.

Power (μW)	A_0	τ_0 (ps)	A_1	τ_1 (ps)	A_2	τ_2 (ps)	A_3	τ_3 (ps)
2	100%	0.5080	44.28%	96.35	25.92%	2656	29.80%	> 8000
3	100%	0.5007	42.86%	85.22	25.51%	2064	31.63%	> 8000
4	100%	0.4977	44.08%	77.25	25.10%	1652	30.82%	> 8000
5	100%	0.4819	45.81%	65.33	25.15%	1471	29.04%	> 8000
6	100%	0.4793	46.08%	68.15	25.49%	1470	28.43%	> 8000

TABLE S2. Fit results of the kinetics probed at 562 nm upon 800 nm excitation.

Power (μW)	A_0	τ_0 (ps)	A_1	τ_1 (ps)	A_2	τ_2 (ps)	A_3	τ_3 (ps)
2	100%	1.316	34.56%	197.5	30.32%	3077	35.12%	> 8000
4	100%	1.113	33.69%	150.7	29.30%	2118	37.01%	> 8000
5	100%	1.025	28.53%	117.8	30.81%	1694	40.66%	> 8000
7	100%	0.8751	26.22%	86.38	31.13%	1576	42.65%	> 8000
8	100%	0.8138	27.33%	77.31	31.42%	1586	41.25%	> 8000

References

- ¹G. Kresse and J. Hafner, “*Ab initio* molecular dynamics for liquid metals,” Phys. Rev. B **47**(1), 558–561 (1993).
- ²P. E. Blöchl, “Projector augmented-wave method,” Phys. Rev. B **50**(24), 17953–17979 (1994).
- ³S. Grimme, J. Antony, S. Ehrlich, and H. Krieg, “A consistent and accurate *ab initio* parametrization of density functional dispersion correction (DFT-D) for the 94 elements H–Pu,” J. Chem. Phys. **132**(15), 154104 (2010).
- ⁴A. Togo, “First-principles phonon calculations with phonopy and phono3py,” J. Phys. Soc. Jpn. **92**(1), 012001 (2023).